PNAS RESEARCH ARTICLE | SUSTAINABILITY SCIENCE OPEN ACCESS

Engineering the interfacial orientation of MoS_2/Co_9S_8 bidirectional catalysts with highly exposed active sites for reversible Li-CO_2 batteries

Bingyi Lu[a,b,1], Biao Chen[a,c,1], Dashuai Wang[a,d,e,1], Chuang Li[a], Runhua Gao[a], Yingqi Liu[a], Rui Mao[a], Jinlong Yang[b,2], and Guangmin Zhou[a,2]

Edited by Alexis Bell, University of California, Berkeley, CA; received October 4, 2022; accepted December 5, 2022

Sluggish CO_2 reduction reaction (CO_2RR) and evolution reaction (CO_2ER) kinetics at cathodes seriously hamper the applications of Li-CO_2 batteries, which have attracted vast attention as one kind of promising carbon-neutral technology. Two-dimensional transition metal dichalcogenides (TMDs) have shown great potential as the bidirectional catalysts for CO_2 redox, but how to achieve a high exposure of dual active sites of TMDs with CO_2RR/CO_2ER activities remains a challenge. Herein, a bidirectional catalyst that vertically growing MoS_2 on Co_9S_8 supported by carbon paper (V-MoS_2/Co_9S_8@CP) has been designed with abundant edge as active sites for both CO_2RR and CO_2ER, improves the interfacial conductivity, and modulates the electron transportation pathway along the basal planes. As evidenced by the outstanding energy efficiency of 81.2% and ultra-small voltage gap of 0.68 V at 20 μA cm^{-2}, Li-CO_2 batteries with V-MoS_2/Co_9S_8@CP show superior performance compared with horizontally growing MoS_2 on Co_9S_8 (H-MoS_2/Co_9S_8@CP), MoS_2@CP, and Co_9S_8@CP. Density functional theory calculations help reveal the relationship between performance and structure and demonstrate the synergistic effect between MoS_2 edge sites and Co_9S_8. This work provides an avenue to understand and realize rationally designed electronic contact of TMDs with specified crystal facets, but more importantly, provides a feasible guide for the design of high-performance cathodic catalyst materials in Li-CO_2 batteries.

bifunctional catalyst | Li-CO_2 batteries | interfacial orientation | reaction path

Rechargeable metal–gas batteries with an energy density of 5 to 10 times beyond that of traditional lithium-ion batteries have attracted widespread attention (1–5). Among these advanced metal–gas batteries, Li-CO_2 battery, based on the reaction of $3CO_2$ (g) + 4Li (s) + $4e^- \leftrightarrow 2Li_2CO_3$ (s) + C (s), is a potential candidate due to high discharge voltages (~2.8 V) and large theoretical specific energy (1,876 Wh kg^{-1}) (6–8). More importantly, Li-CO_2 batteries not only act as one kind of promising carbon-neutral technology to provide a method of CO_2 fixation for serious global warming, but also offer opportunity for applications such as Mars exploration or submarine operations with CO_2-rich environments (9–11).

Despite the great potential of Li-CO_2 batteries, there are some thorny problems (12). One of the challenges is that the sluggish CO_2 reduction reaction (CO_2RR) and evolution reaction (CO_2ER) kinetics at cathodes seriously deteriorate the performance of the Li-CO_2 batteries. The CO_2RR and CO_2ER involve a conversion from gas to two solids in liquid electrolyte, and the insulating nature of the discharge product lithium carbonate makes its formation and decomposition exceptionally difficult (13–15). The unexpected irreversible conversion reaction leads to poor reversibility and low energy efficiency. Therefore, the construction of unique electrode structures with efficient bidirectional catalysts to facilitate the reduction of CO_2 and the oxidation of the discharge products is of particular importance.

Two-dimensional transition metal dichalcogenides (TMDs) are an interesting family of layered materials that have been widely studied in various fields such as electrocatalysis, metal–sulfur batteries, and Li-O_2/-CO_2 batteries, due to their unique physical and chemical properties (8, 16–17). However, the basal planes of most semiconducting TMDs have poor intrinsic activity, which is much smaller than that of the edge sites (18–20). To address this problem, surface engineering, including defect, doping, and single-atom decoration has been applied to improve electrical conductivity and activate surface activity (21–25). For example, nucleophilic N dopants and electrophilic S vacancies in the ReS_2 plane have been designed to promote the bidirectional activity in Li-CO_2 batteries (21). However, for achieving bidirectional catalysis in Li-CO_2 batteries, the precise synthesis of dual active centers in the basal plane through surface engineering is still hard to control (26). In this regard, developing a new strategy to minimally expose the basal plane of TMDs shows highly desirable for their use in Li-CO_2 batteries.

Significance

Li-CO_2batteries not only act as promising carbon-neutral technology to provide a method of CO_2fixation for serious global warming, but also offer opportunity for applications such as Mars exploration or submarine operations with CO_2-rich environments. We design an efficient bifunctional activity in 2D materials with a large number of dual active centers, realizing highly reversible Li-CO_2batteries with an ultra-small voltage gap of 0.68 V and an ultra-high energy efficiency of 81.2%, which is superior to those of previous catalysts under similar conditions. This work not only paves an avenue to understand and realize rationally manipulated electronic contact of 2D materials with specified crystal facets, but also offers guidance for designing high-performance catalysts for Li-CO_2batteries.

Author contributions: B.L. and G.Z. designed research; B.L., B.C. and D.W. performed research; B.L., B.C., D.W., C.L., R.G., Y.L., R.M., J.Y., and G.Z. analyzed data; and B.L., B.C., D.W., J.Y., and G.Z. wrote the paper.

The authors declare no competing interest.

This article is a PNAS Direct Submission.

[1]B.L., B.C. and D.W. contributed equally to this work.

[2]To whom correspondence may be addressed. Email: yangjl18@szu.edu.cn or guangminzhou@sz.tsinghua.edu.cn.

This article contains supporting information online at https://www.pnas.org/lookup/suppl/doi:10.1073/pnas.2216933120/-/DCSupplemental.

Published January 30, 2023.

Recently, edge engineering has attracted emerging attention, in which TMDs grew perpendicular to the substrates, thereby maximally exposing the highly active edge sites, and showing excellent intrinsic activity for catalytic reactions (27). Meanwhile, the interfacial interactions between substrate and vertically aligned TMD nanosheets are strong, leading to a fast electron transport path from the substrate to edge sites (28). As far as CO_2RR and CO_2ER in Li-CO_2 batteries, the reported edge-terminated films did not exist, and the fast CO_2/electrolyte diffusion, the enough space for accommodating discharged products, and a large number of active sites are also important to promote reaction kinetics. In addition, two kinds of active sites are more favorable to achieving excellent and stable bidirectional activity, thereby incorporating another promising active material with vertically aligned TMDs is urgently needed. The key challenge in producing excellent TMD-based bidirectional catalysts for reversible Li-CO_2 batteries is how to achieve freestanding TMD-based cathode with maximally exposing edge sites, a large number of dual active sites, porous structure, good electrical conductivity, and strong interfacial interaction.

In this work, we design a freestanding cathode, in which ultrasmall MoS_2 vertically grows on Co_9S_8 sheets supported by carbon paper with a large number of exposed active sites (V-MoS_2/Co_9S_8@CP). Notably, the designed freestanding V-MoS_2/Co_9S_8@CP cathode shows all above-mentioned good properties for achieving excellent bidirectional catalysts (Fig. 1*A*). Moreover, structure–performance relationship, MoS_2 edge sites and Co_9S_8 active sites decrease the energy barriers for different rate-determining steps, which show the obviously complementary effect to facilitate the reaction kinetics revealed by density functional theory (DFT) calculations. As a result, the Li-CO_2 battery assembled with V-MoS_2/Co_9S_8@CP delivers superior performances of an ultra-small voltage gap (0.68 V) and high energy efficiency (81.2%) at 20 μA cm^{-2}.

Results and Discussion

Synthesis and Characterization of Free-standing Catalysts. The V-MoS_2/Co_9S_8@CP is prepared by a two-step procedure, as shown in *SI Appendix*, Fig. S1. First, Mo-$Co(CO_3)_{0.5}OH{\cdot}0.11H_2O$ nanosheets vertically anchored on the surface of carbon paper by hydrothermal method [Mo-$Co(CO_3)_{0.5}OH{\cdot}0.11H_2O$/CP, *SI Appendix*, Fig. S2]. Then, the gaseous sulfur reacted with Mo-$Co(CO_3)_{0.5}OH{\cdot}0.11H_2O$ nanosheets from surface to interface to prepare MoS_2/Co_9S_8 heterostructure (V-MoS_2/Co_9S_8@CP), which keep vertical structure on the surface of CP. During the sulfurization, because the growth directions of Co_9S_8 are isotropic, the Co_9S_8 inherits the sheet morphology of oxides. For MoS_2, due to the weak Van der Walls interaction between MoS_2 layers, the sulfurization direction is parallel to the basal plane (29). The growth of MoS_2 nanosheets is along the direction from the surface to interface (30). Therefore, in the obtained MoS_2/Co_9S_8 heterostructure, the MoS_2 nanosheets vertically grow on the surface of Co_9S_8 sheets with an interface along the edge of MoS_2. The structure of V-MoS_2/Co_9S_8@CP was studied by scanning electron microscopy (SEM) and transmission electron microscopy (TEM). As shown in Fig. 1*B*, the surface of CP was fully and uniformly covered by sheets. The vertical sheets have ultrathin thickness, and they are cross-linked to form porous structure, which facilitates the transport of CO_2 gas and provides a large specific surface area to accommodate discharge products (31–32). The TEM image (Fig. 1*C*) and inserted fast Fourier transform (FFT) pattern show that MoS_2 nanosheets with four to eight layers vertically stand on Co_9S_8 surface with exposed (01–1) plane. High-resolution TEM (HRTEM) image reveals that the size of the vertically aligned MoS_2 nanosheets is around ~5 nm (Fig. 1*D*). Furthermore, the MoS_2 nanoplate is seamlessly bonded to Co_9S_8 surface along the edges and fringes with a lattice spacing of 6.15 Å, while that of Co_9S_8 is 2.98 Å, corresponding to the (002) plane of hexagonal MoS_2 and (311) of Co_9S_8, respectively. The coexistence of MoS_2 and Co_9S_8 is further confirmed by selected area electron diffraction (SAED) patterns (inset image in Fig. 1*D*). As illustrated in Fig. 1*E*, the MoS_2 with exposed (002) plane vertically stands on the (01-1) planes of Co_9S_8. Moreover, the X-ray energy-dispersive spectroscopy (EDS) elemental mapping images show that the Co, Mo, and S elements are uniformly distributed through the nanosheet morphology (Fig. 1*F*). For comparison, the MoS_2 nanosheets vertically anchored on CP (MoS_2@CP), Co_9S_8 nanosheets vertically anchored on CP (Co_9S_8@CP) and MoS_2 horizontally lie on Co_9S_8 heterostructures that anchored on CP (H-MoS_2/Co_9S_8@CP) were also prepared. Their detailed synthesis processes are shown in *SI Appendix*, Supporting Information. Their microstructures were investigated by SEM images, as shown in *SI Appendix*, Figs. S3–S5.

The composition, phase, and chemical states of the four samples were further investigated. The X-ray diffraction (XRD) measurements show the phases of all the obtained samples agree well with their standard PDF cards (MoS_2: 37-1492 and Co_9S_8: 19-0364), together with the intensive carbon peak at about 26° (*SI Appendix*, Fig. S6). As shown in Raman spectra of Fig. 1*G*, the stretching vibration bands of MoS_2 corresponding to E_{2g} (in-plane) and A_{1g} (out-of-plane) are observed at 373.90 and 401.67 cm^{-1}, respectively. The characteristic vibration bands of Co_9S_8 are located at 188.30, 467.84, and 512.40 cm^{-1}. All these bands corresponding to Co_9S_8 and MoS_2 can be found in V-MoS_2/Co_9S_8@CP, confirming the successful fabrication of the MoS_2/Co_9S_8 heterostructure. X-ray photoelectron spectroscopy (XPS) was used to analyze the chemical states (Fig. 1 *H* and *I* and *SI Appendix*, Figs. S7 and S8) (33). Fig. 1 *H* and *I* show the high-resolution XPS spectra of Mo 3d and Co 2p. For Mo 3d spectra; the peaks of Mo^{4+} $3d^{3/2}$ and Mo^{4+} $3d^{5/2}$ are, respectively, located at 232.59 eV and 229.21 eV for V-MoS_2/Co_9S_8@CP, while 232.65 eV and 229.53 eV for MoS_2@CP. For Co 2p spectra, they can be deconvoluted into six peaks, including Co^{2+} (798.58 eV and 782.24 eV), Co^{3+} (793.93 eV and 778.94 eV), and satellite peaks (803.39 eV and 786.21 eV) for V-MoS_2/Co_9S_8@CP. The peaks of Co^{2+} are at 797.38 eV and 781.42 eV, and the peaks of Co^{3+} are at 793.29 eV and 778.4 eV in Co_9S_8@CP. Compared to V-MoS_2/Co_9S_8@CP, Mo^{4+} undergoes a negative shift and Co (Co^{2+} and Co^{3+}) experiences a positive shift, suggesting strong electronic interaction between Co_9S_8 and MoS_2, as well as the formation of the heterojunction (34, 35). Moreover, for the S 2p spectra, two peaks at 161.98 and 163.12 eV correspond to S $2p^{3/2}$ and S $2p^{1/2}$, respectively (*SI Appendix*, Fig. S8). Besides, the peak at 164.59 eV confirms the presence of bridging disulfides S_2^{2-} in V-MoS_2/Co_9S_8@CP.

Electrochemical Performance in Li-CO_2 Batteries. To testify the electrochemical performance of four free-standing cathodes, corresponding Li-CO_2 batteries were assembled. The cyclic voltammetry (CV) tests were firstly conducted in the range between 2.2 and 4.5 V under CO_2 atmosphere (Fig. 2*A*). Furthermore, the CO_2RR and CO_2ER kinetics were evaluated by the onset potentials corresponding to 40 μA cm^{-2} in Fig. 2*B*. V-MoS_2/Co_9S_8@CP shows a cathodic onset potential of 2.92 V, which is higher than Co_9S_8@CP (2.76 V), MoS_2@CP (2.77 V) and H-MoS_2/Co_9S_8@CP (2.82 V). The anodic onset potentials of V-MoS_2/Co_9S_8@CP, Co_9S_8@CP, MoS_2@CP, and H-MoS_2/Co_9S_8@CP are 3.50, 3.94, 3.44, and 3.80 V, respectively. The anodic initial potential of V-MoS_2/Co_9S_8@CP is similar to that of MoS_2@CP, but it is significantly smaller than that of the other two catalysts. The above results suggest

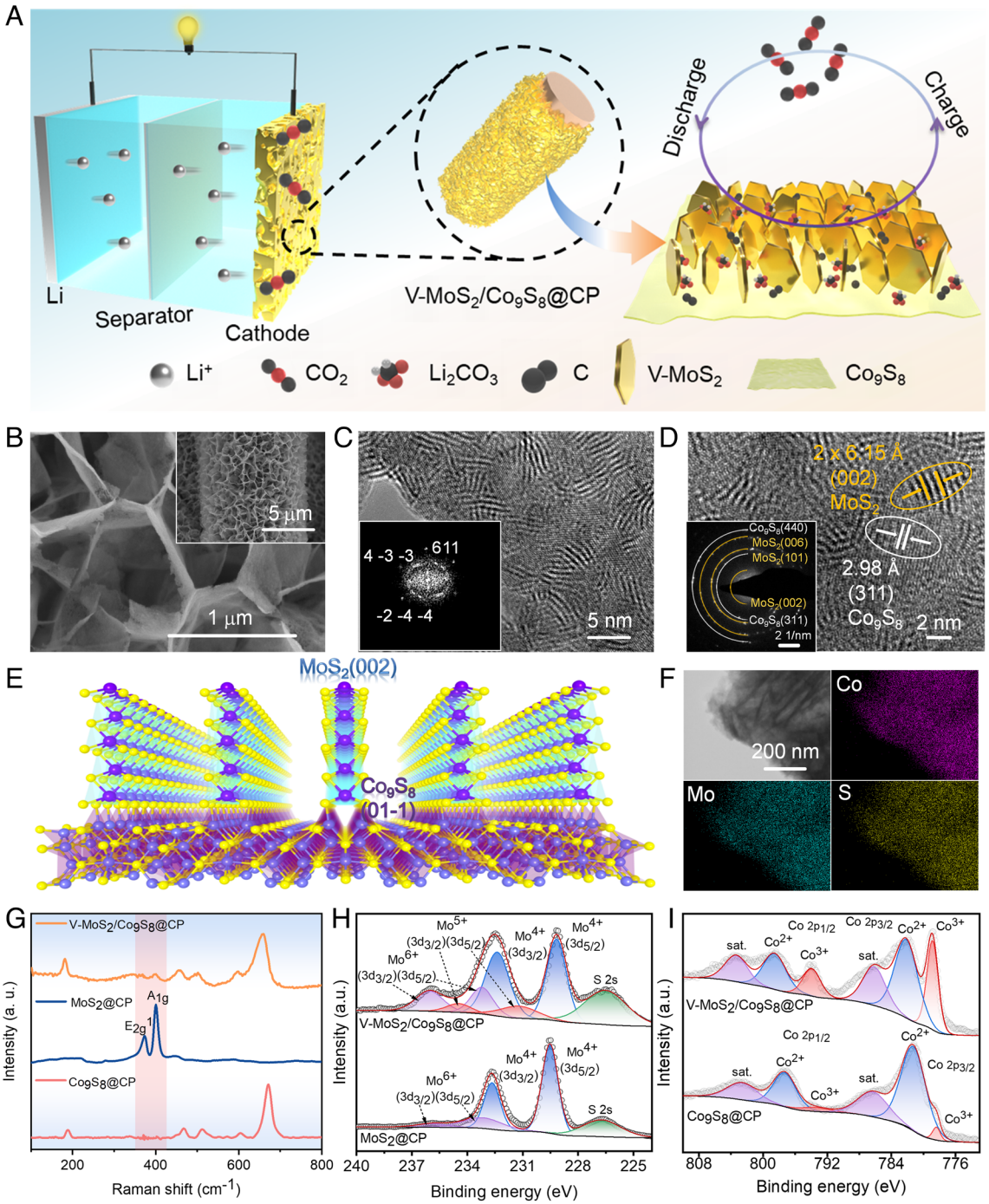

Fig. 1. (*A*) Illustration of V-MoS_2/Co_9S_8@CP in Li-CO_2 batteries. (*B*) SEM, (*C*) TEM, (*D*) HRTEM images of V-MoS_2/Co_9S_8@CP. (*E*) Illustration of the V-Co_9S_8/MoS_2@CP with MoS_2 vertically grows on Co_9S_8 with an interface along the edge. (*F*) EDS-mapping images of V-MoS_2/Co_9S_8@CP. (*G*) Raman spectra and (*H* and *I*) XPS fine spectra of V-Co_9S_8/MoS_2@CP, Co_9S_8@CP, and MoS_2@CP. The inserted images in *C* and *D* are FFT pattern and SAED image of Co_9S_8 and V-MoS_2/Co_9S_8, respectively.

that V-MoS_2/Co_9S_8@CP cathode has better CO_2RR and CO_2ER kinetics than the other three cathodes. Full discharge profiles are displayed in Fig. 2*C*. V-MoS_2/Co_9S_8@CP cathode delivers a full discharge capacity of 3,954 μA h cm^{-2} with a discharge plateau at ~2.80 V. They are both higher than those of Co_9S_8@CP (1039 μA h cm^{-2} and 2.78 V), MoS_2@CP (548 μA h cm^{-2} and 2.53 V) and H-MoS_2/Co_9S_8@CP (885 μA h cm^{-2} and 2.61 V). The V-MoS_2/Co_9S_8@CP cathode retains a high Coulombic efficiency of 71% after charging (*SI Appendix*, Fig. S9), suggesting a high bidirectional activity in Li-CO_2 batteries. Therefore, the V-MoS_2/Co_9S_8@CP cathode shows the best catalytic kinetics and the largest number of available active sites among all the catalysts.

The rate capabilities and cycling stability of the Li-CO_2 batteries with the four as-obtained cathodes were tested with a limited capacity of 100 μAh cm^{-2}. For the galvanostatic discharge–charge (GDC) profiles at different current densities, as shown in Fig. 2 *D*–*F* and *SI Appendix*, Figs. S10–S12, the V-MoS_2/Co_9S_8@CP cathode shows superior rate performance, with voltage gaps of 0.68, 0.86, 1.07, and 1.33 V and energy efficiencies of 81.2, 77.0, 72.2, and 66.7% at 20, 40, 70, and 100 μA cm^{-2}, respectively. The V-MoS_2/Co_9S_8@CP cathode shows higher median discharge voltages, smaller voltage gaps, and higher energy efficiencies than those of the Co_9S_8@CP, MoS_2@CP, and H-MoS_2/Co_9S_8@CP at the same condition (*SI Appendix*, Table S1). When the current

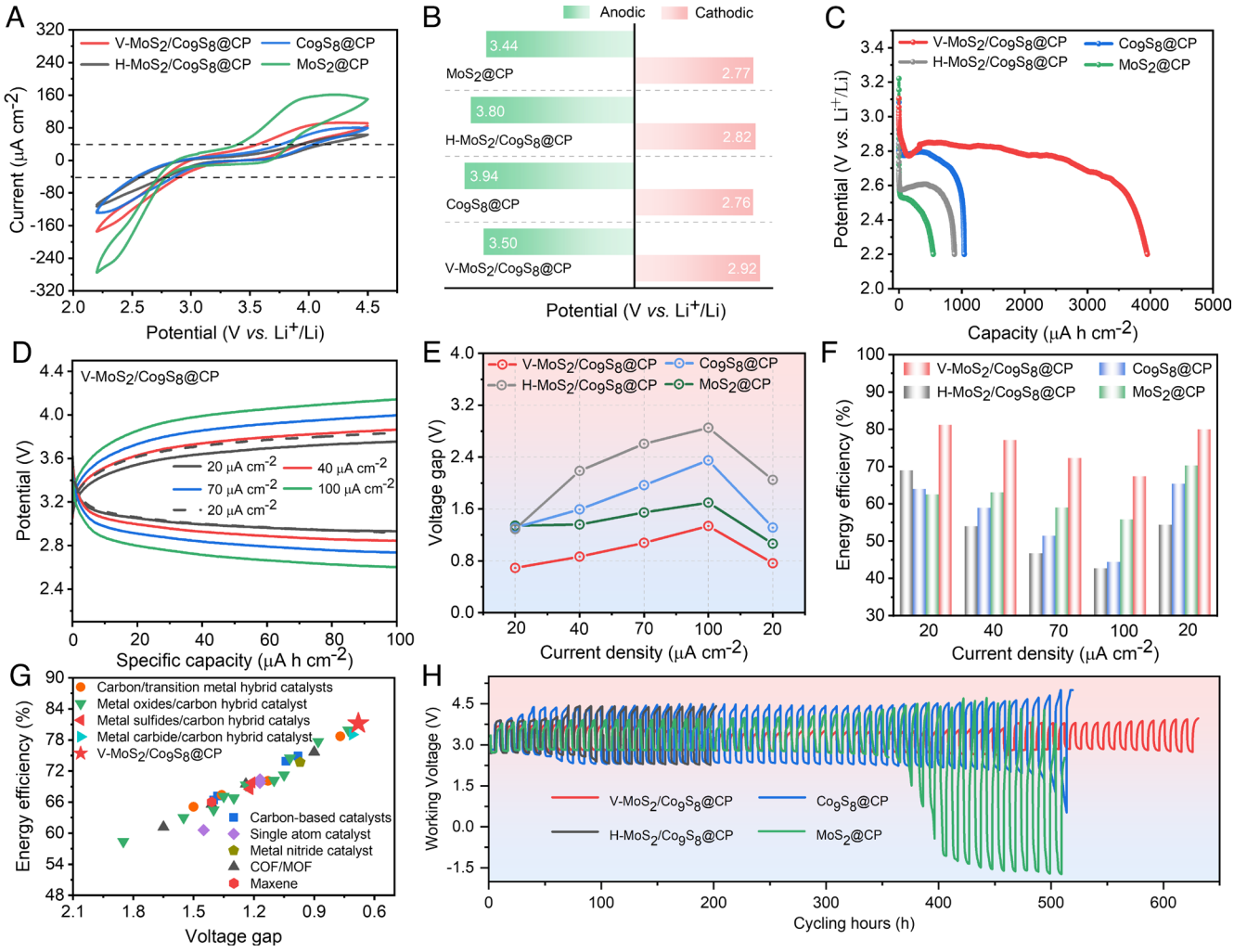

Fig. 2. (*A*) CV curves at a scanning rate of 0.2 mV s^{-1}, (*B*) corresponding onset potentials during discharging and charging, and (*C*) fully discharging curves of four cathodes at 40 μA cm^{-2}. (*D*) GDC profiles with a limited capacity of 100 μA h cm^{-2} at different current densities for V-MoS_2/Co_9S_8@CP. (*E*) Voltage gaps and (*F*) energy efficiencies at different current densities for four cathodes. (*G*) Performance comparison chart, voltage gaps and energy efficiencies for rechargeable Li-CO_2 batteries with V-MoS_2/Co_9S_8@CP and other reported catalysts. (*H*) Cycling performance of four cathodes at 20 μA cm^{-2}.

density recovers back to the initial value, the median discharge voltage and median charge voltage are almost the same as the initial constant, demonstrating that the V-MoS_2/Co_9S_8@CP has excellent reversibility. Moreover, compared with cathode catalysts previously reported (the discharge time ≥5 h), V-MoS_2/Co_9S_8@CP cathode also exhibits superior performance regarding with voltage gap and energy efficiency under similar conditions (Fig. 2*G* and *SI Appendix*, Table S2). Moreover, the V-MoS_2/Co_9S_8@CP cathode shows stable long-term cycling stability at different current densities (20 and 40 μA cm^{-2}) (Fig. 2*H* and *SI Appendix*, Figs. S13 and S14). The V-MoS_2/Co_9S_8@CP cathode maintains a high discharge voltage of 2.81 V and a low charge voltage of 3.85 V after 630 h at 20 μA cm^{-2}. Attractively, the V-MoS_2/Co_9S_8@CP cathode can be reversibly charged and discharged for 140 h at 40 μA·cm^{-2} with a relatively stable discharge and charge plateau (*SI Appendix*, Fig. S14), demonstrating good cycling stability. In addition, V-MoS_2/Co_9S_8@CP cathode exhibits the smallest voltage gaps and the largest energy efficiencies in the overall cycling life among all cathodes, which are consistent with the results of rate performance. The above results show that the V-MoS_2/Co_9S_8@CP exhibits excellent bidirectional catalytic activity towards CO_2RR and CO_2ER processes, resulting in reversible conversion reactions and high energy efficiencies in Li-CO_2 batteries.

High Reversibility and Stability of V-MoS_2/Co_9S_8@CP Cathode. To uncover the conversion reaction mechanism of V-MoS_2/Co_9S_8@CP cathode in Li-CO_2 batteries, ex situ XRD and SEM measurements at different working states in the first cycle were conducted (Fig. 3 *A*–*E* and *SI Appendix*, Figs. S15–S19). As shown in Fig. 3*C*, the granular Li_2CO_3 is readily observed during discharge, and in the following charge process, which is almost no residue on the surface of V-MoS_2/Co_9S_8@CP cathode after the first cycle. It is in sharp contrast to the cases containing H-MoS_2/Co_9S_8@CP, Co_9S_8@CP and MoS_2@CP, for which there still exist many particle residues (Fig. 3*D* and *SI Appendix*, Figs. S16 and S17). Ex situ XRD patterns show that the Li_2CO_3 signal emerges and was easily observed from XRD patterns during discharge. During the subsequent charging process, the signal in V-MoS_2/Co_9S_8@CP cathode is gradually weakened and has disappeared in the final state, while the obvious signal of Li_2CO_3 can still be detected in H-MoS_2/Co_9S_8@CP, Co_9S_8@CP and MoS_2@CP cathodes (Fig. 3*E* and *SI Appendix*, Figs. S15, S16 *B*, S17 *B*, and S19). This suggests that the V-MoS_2/Co_9S_8@CP has an excellent bidirectional activity for both CO_2RR and CO_2ER. Moreover, TEM and XPS were used to investigate the stability of V-MoS_2/Co_9S_8@CP after repeated cycles at 20 μA cm^{-2} (Fig. 3 *F* and *G*, and *SI Appendix*, Figs. S20 and S21). As revealed, the V-MoS_2/Co_9S_8@CP remains in its sheet structure, in which MoS_2 nanosheets vertically stand on the surface of Co_9S_8 sheets and

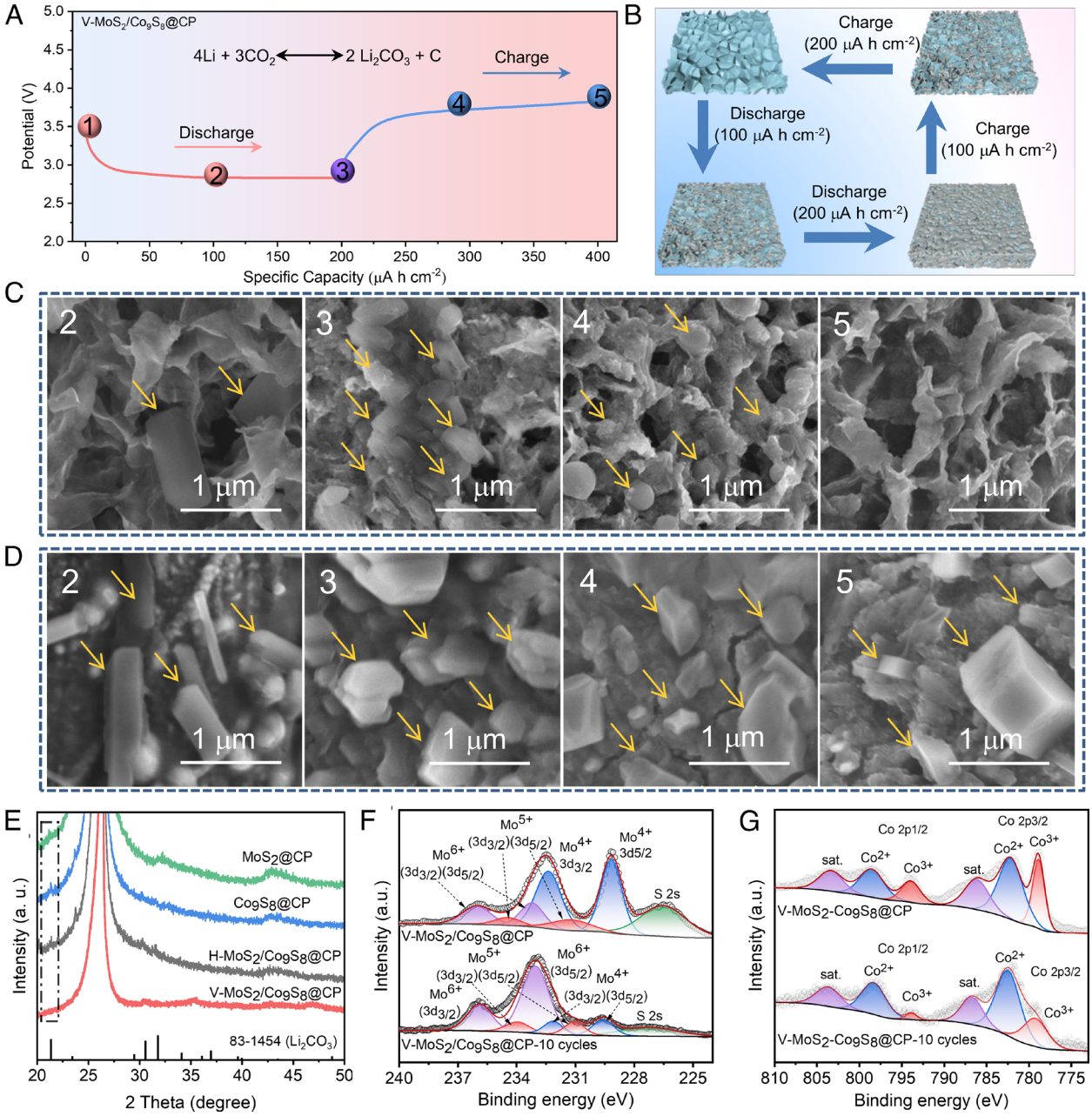

Fig. 3. (*A*) GDC profiles of V-MoS_2/Co_9S_8@CP cathode at 20 μA cm^{-2} with a capacity limit of 200 μA h cm^{-2}. The labels 1 to 5, respectively, represent the electrochemical states of pristine, discharging with 100, 200, and charging with 100, 200 μA h cm^{-2}. (*B*) Schematic illustration of the morphological changes. (*C* and *D*) SEM images at the different working states for V-MoS_2/Co_9S_8@CP and H-MoS_2/Co_9S_8@CP cathodes, respectively. (*E*) Ex situ XRD patterns for four cathodes when charged to 200 μA h cm^{-2}. (*F* and *G*) Mo 3d and Co 2p XPS spectra of V-Co_9S_8/MoS_2@CP and V-Co_9S_8/MoS_2@CP cathode after 10 cycles.

the Co, Mo, and S elements are uniformly distributed in the sheet structure after 10 cycles. Furthermore, the chemical states of Mo 3d and Co 2p spectra in V-MoS_2/Co_9S_8@CP after 10 cycles show a little change when compared with those in pristine V-MoS_2/Co_9S_8@CP, suggesting high chemical stability during repeated CO_2RR and CO_2ER. These results verify that V-MoS_2/Co_9S_8@CP possesses excellent bidirectional activity, robust structure, and high stability for its full play as the catalyst for CO_2 redox.

To get deep insight into the effect of V-MoS_2/Co_9S_8@CP cathode in the Li-CO_2 battery, in situ differential electrochemical mass spectrometry (DEMS) was applied to investigate the gas evolution during discharge–charge process at a high current of 150 μA (36–39). The V-MoS_2/Co_9S_8@CP cathode shows a higher discharge voltage and a lower charge voltage, which is in sharp contrast to the other cathode materials (Fig. 4 *A*–*H*). In the discharge process, the molar amount of charge lost is 5.60×10^{-6} mol. According to the typical CO_2RR: $3CO_2 + 4e^- + 4Li^+ \rightarrow 2Li_2CO_3 + C$, the theoretical CO_2 mass-to-charge ratio is 0.75, so the theoretical mole number of CO_2 is 4.19×10^{-6} mol. The moles of CO_2 consumed by V-MoS_2/Co_9S_8@CP, H-MoS_2/Co_9S_8@CP, Co_9S_8@CP, and MoS_2@CP in the discharge process can be calculated by area integral, and they are 3.99×10^{-6}, 2.16×10^{-6}, 1.38×10^{-6}, and 3.64×10^{-6} mol, respectively. The efficiency of CO_2 reduction of V-MoS_2/Co_9S_8@CP, H-MoS_2/Co_9S_8@CP, Co_9S_8@CP and MoS_2@CP cathodes are 95.2%, 51.6%, 33.0%, and 86.9%, respectively. Moreover, no CO was traced during CO_2RR. In the charge process, the amount of CO_2 evolution in the V-MoS_2/Co_9S_8@CP cathode is much higher than that of the others. Meanwhile, no O_2, NO, NO_2, and SO were detected (Fig. 4 *B*, *D*, *F* and *H*), which ruled out the self-decomposition of Li_2CO_3 and the

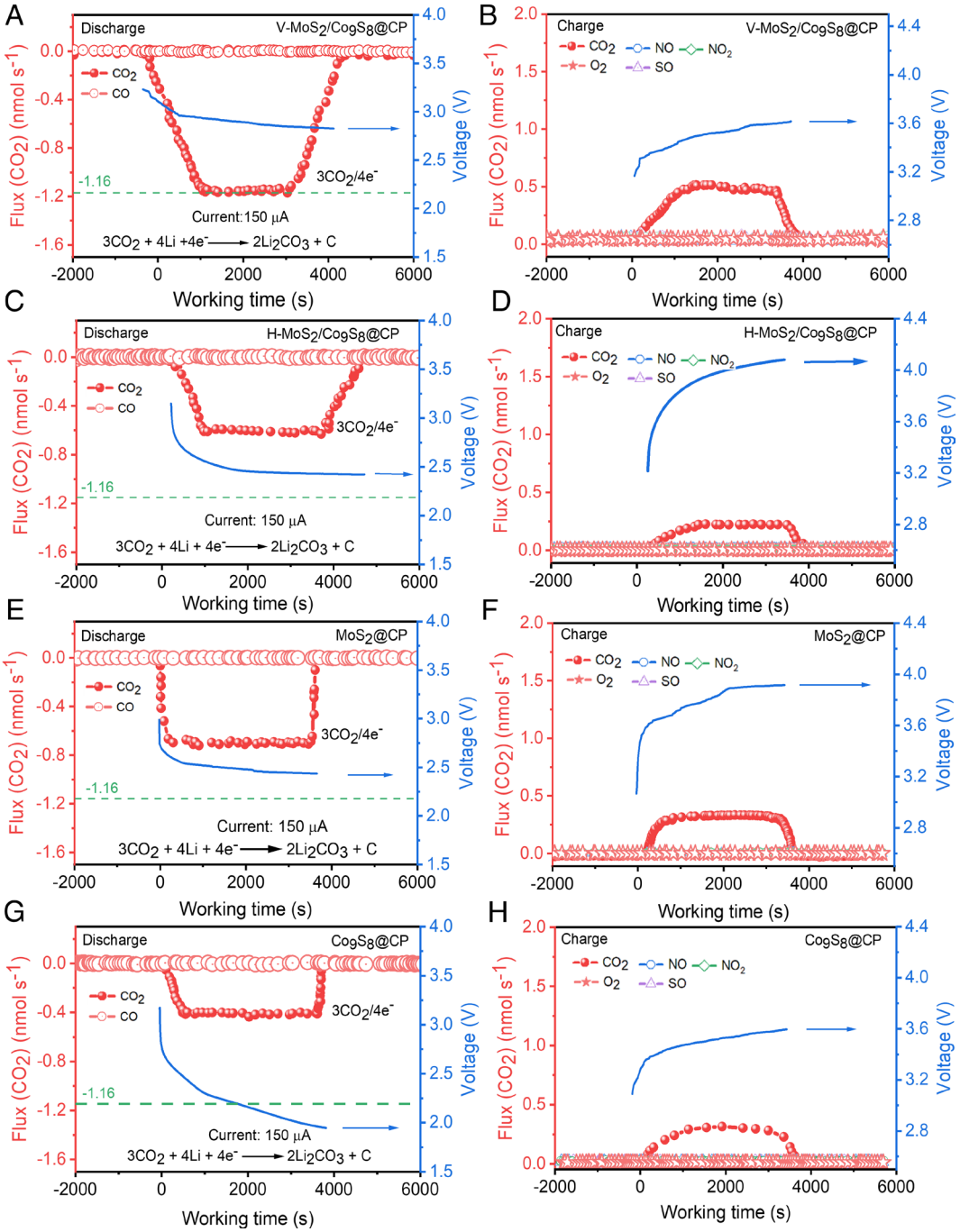

Fig. 4. DEMS profiles with discharge-charge curves at a current of 150 μA for (*A* and *B*) V-MoS_2/Co_9S_8@CP, (*C* and *D*) H-MoS_2/Co_9S_8@CP, (*E* and *F*) MoS_2@CP, and (*G* and *H*) Co_9S_8@CP cathodes.

occurrence of side reactions. The above results clearly suggest that V-MoS_2/Co_9S_8@CP has excellent catalytic activity, which was consistent with the results of electrochemical performance test.

The Origin of the Excellent Bifunctional Activity from DFT Calculations. DFT calculations were further used to explore the origin of catalytic activity of CO_2RR and CO_2ER of the V-MoS_2/Co_9S_8@CP cathode. Three models, including Co_9S_8, MoS_2 basal plane, and MoS_2 edge, were constructed (20). It is found that the bonding strength of MoS_2 plane and edge with Co_9S_8 (01–1) plane is −0.23 and −0.05 eV/Å^2, respectively. Meanwhile, according to the corresponding differential charge density (*SI Appendix*, Fig. S22), it can be found that the bonding number of Co_9S_8 (01-1) planes and MoS_2 edges are more than that of MoS_2 basal planes. These results suggest that (01-1) planes of Co_9S_8 are selective for vertically growing MoS_2. We first investigated the adsorption configurations of CO_2, Li, and Li_2CO_3, and resulting charge density differences on three models (Fig. 5 *A* and *B* and *SI Appendix*, Figs. S23–S28). For CO_2RR, the strong adsorption ability for CO_2 and Li is a crucial role in the activation stage of reactants. As shown in Fig. 5*C*, MoS_2 edge reveals higher adsorption energy for CO_2 and Li in contrast to the MoS_2 basal plane and Co_9S_8. Therefore, the fully exposed MoS_2 edge endows the V-MoS_2/Co_9S_8@CP with stronger adsorption energy toward CO_2 and Li, so as to achieve better catalytic performance for the CO_2RR. Meanwhile, the intrinsic activities of MoS_2 edge, MoS_2 basal plane and Co_9S_8 were studied. We calculated the Gibbs free energy (ΔG_f) for eight possible reaction pathways, which can be

divided into two reaction stages (40). As shown in *SI Appendix*, Fig. S29, in the first stage, *Li_2CO_3 and *CO (* represents the catalytic surface) were formed through five possible reaction paths, and finally Li_2CO_3 and C were formed after the second stage. The ΔG_f at both U = 0 V (open-circuit potentials) and U = U_0 = 2.85 V (equilibrium potentials) were calculated for five possible pathways (*SI Appendix*, Figs. S30–S32 and Tables S3–S5) (41). MoS_2 basal plane, MoS_2 edge and Co_9S_8 show different reaction paths, and the most favorable paths for three materials are I, IV and II, respectively (Fig. 5*D* and *SI Appendix*, Fig. S33). In the first stage, Gibbs free energy changes at the rate-determining step [$\Delta G_f(r)$] of MoS_2 base plane, MoS_2 edge, and Co_9S_8 are 2.67, 1.70, and 0.93 eV, respectively. Obviously, Co_9S_8 shows the smallest value, which means that it exhibits the best thermodynamics during the formation of Li_2CO_3 and *CO. In the second stage, MoS_2 edge displays the smallest $\Delta G_f(r)$ (2.87 eV), followed by Co_9S_8 and MoS_2 basal plane, which were 5.2 and 6.09 eV, respectively (Fig. 5*E* and *SI Appendix*, Table S6). The fully exposed MoS_2 edges and Co_9S_8 in the V-MoS_2/Co_9S_8@CP show complementary effects, leading to significantly reduced energy barriers of the rate-determining steps. The complementary effect of the two kinds of active sites promotes the reaction kinetics, leading to excellent catalytic activity. Compared with the edge of MoS_2 and Co_9S_8, the MoS_2 basal plane has bigger $\Delta G_f(r)$ in both stages, which is not conducive to the progress of CO_2RR. The calculated results of ΔG_f are consistent with the experimental results, which to a certain extent indicates the effective design of the dual-active sites catalyst.

In terms of CO_2ER, the crucial step is the decomposition of Li_2CO_3, which can be reflected by the bond type of adsorbing Li_2CO_3 (42, 43). In the MoS_2 basal plane, the Li_2CO_3 is adsorbed through the Li-S bonds while MoS_2 edges and Co_9S_8 through Li-S bonds and Mo-O or Co-O bonds. The addition of Mo-O or Co-O bonds can further weaken the interaction between Li-O bonds, thereby achieving a favorable decomposition of Li_2CO_3 (*SI Appendix*, Fig. S25). Furthermore, the sequentially increased electron depletion of Li-O bonds also verifies that the bond strength of Li-O bonds weakened. As a result, the V-MoS_2/Co_9S_8@CP exhibit the highest catalytic ability for the decomposition of Li_2CO_3, followed by Co_9S_8@CP, and MoS_2@CP is the weakest as depicted in Fig. 5 *F* and *G* and *SI Appendix*, Fig. S34. These results further support the effective design of V-MoS_2/Co_9S_8@CP catalyst for Li-CO_2 batteries.

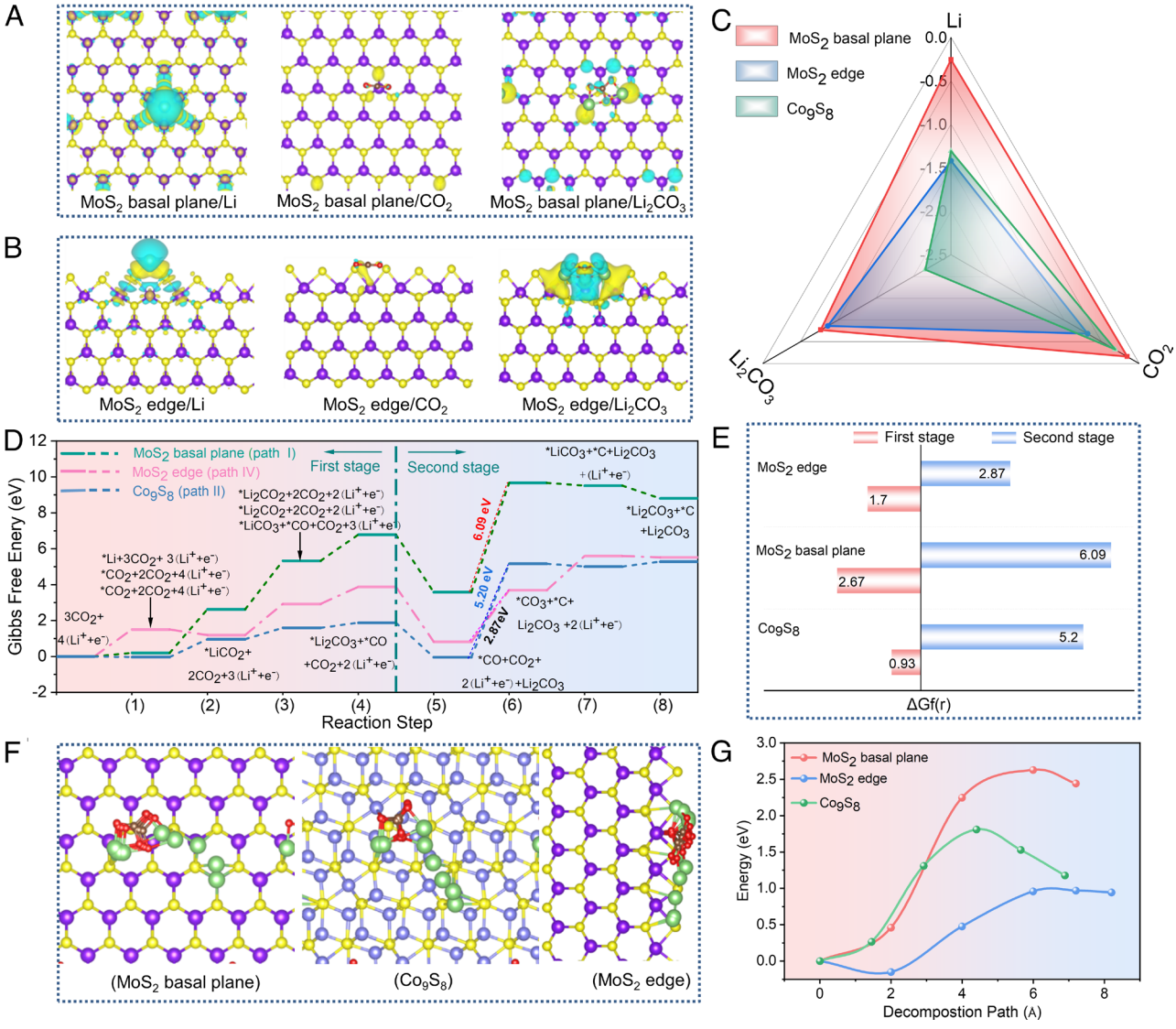

Fig. 5. Top views for the charge density difference of Li, CO_2 and Li_2CO_3 adsorption configurations on (*A*) MoS_2 basal plane and (*B*) MoS_2 edge, respectively. (*C*) Adsorption energies of Li, CO_2 and Li_2CO_3 on the Co_9S_8, MoS_2 basal plane and MoS_2 edge. (*D*) The most favorable paths for MoS_2 basal plane, MoS_2 edge and Co_9S_8, and (*E*) the Gibbs free energy changes at the rate-determining step. (*F*) Detailed decomposition paths and (*G*) decomposition energy barriers of Li_2CO_3 on Co_9S_8, MoS_2 basal plane and MoS_2 edge.

According to the above experimental and theoretical analysis, the synergistic effect of fully exposed MoS_2 edge sites and Co_9S_8 endow V-MoS_2/Co_9S_8@CP with excellent bidirectional catalytic activity. The MoS_2 edge showed high adsorption energies to CO_2 and Li and proper adsorption energies to CO and CO_3 intermediates, while Co_9S_8 plane shows appropriate adsorption energy to $LiCO_3$ and Li_2CO_3 intermediates. According to Gibbs free energy analysis of the reaction process, it can be seen that Co_9S_8 displays the smallest reaction energy barrier in the first stage of the reaction, and the MoS_2 edge presents the smallest reaction energy barrier in the second stage, leading to good reaction kinetics during CO_2RR. During CO_2ER, MoS_2 edge and Co_9S_8 further weaken the interaction between Li-O bond through Li-S bonds and Mo-O or Co-O bonds, to achieve favorable decomposition of Li_2CO_3. The co-existence of MoS_2 edges and Co_9S_8 in V-MoS_2/Co_9S_8@CP gives it bidirectional activities and electrochemical performance in Li-CO_2 batteries.

Conclusion

In summary, we have designed and synthesized a V-MoS_2/Co_9S_8 heterostructure vertically anchored on CP, in which MoS_2 with fully exposed edge sites grows vertically on Co_9S_8. The porous lamellar V-MoS_2/Co_9S_8 nanosheets not only facilitate the diffusion of CO_2 and electrolyte, but also provide a large number of active sites and ample space to accommodate discharge products of Li_2CO_3 and carbon. More importantly, the fully exposed MoS_2 edge and Co_9S_8 have a good synergistic effect on CO_2RR and CO_2ER processes, leading to excellent intrinsic activity, which is demonstrated by both experimental and theoretical results. As a result, the V-MoS_2/Co_9S_8@CP cathode exhibits an excellent energy efficiency of 81.2% and an ultra-small voltage gap of 0.68 V at 20 μA cm^{-2}. This work not only contributes excellent bidirectional catalysts for high-performance Li-CO_2 batteries, but also provides a viable guidance for further developing bidirectional catalysts toward CO_2 electrochemical redox in rechargeable energy storage systems.

Experimental Section

Experimental details and characterizations are included in *SI Appendix*.

Data, Materials, and Software Availability. All study data are included in the article and/or *SI Appendix*.

ACKNOWLEDGMENTS. G.Z. appreciates support from the National Key Research and Development Program of China (2019YFA0705700), Shenzhen Stabilization Support Program (WDZC20200824091903001), Shenzhen Science and Technology Program (KQTD20210811090112002), the Overseas Research Cooperation Fund, and Interdisciplinary Research and Innovation Fund of Tsinghua Shenzhen International Graduate School. We would like to thank the Testing Technology Center of Materials and Devices of Tsinghua Shenzhen International Graduate School for its help with materials characterization.

Author affiliations: [a]Tsinghua-Berkeley Shenzhen Institute & Tsinghua Shenzhen International Graduate School, Tsinghua University, Shenzhen 518055, China; [b]Guangdong Research Center for Interfacial Engineering of Functional Materials, College of Materials Science and Engineering, Shenzhen University, Shenzhen 518060, China; [c]School of Materials Science and Engineering and Tianjin Key Laboratory of Composite and Functional Materials, Tianjin University, Tianjin 300350, People's Republic of China; [d]Institute of Zhejiang University-Quzhou, Quzhou 324000, China; and [e]College of Chemical and Biological Engineering, Zhejiang University, Hangzhou 310027, China

1. J. Zhou *et al.*, Flexible metal-gas batteries: A potential option for next-generation power accessories for wearable electronics. *Energy Environ. Sci.* **13**, 1933–1970 (2020).
2. Y. Huang *et al.*, Atomic modulation and structure design of carbons for bifunctional electrocatalysis in metal-air batteries. *Adv. Mater.* **31**, 1803800 (2019).
3. F. Cheng, J. Chen, Metal-air batteries: From oxygen reduction electrochemistry to cathode catalysts. *Chem. Soc. Rev.* **41**, 2172–2192 (2012).
4. L. Yang *et al.*, Harnessing the surface structure to enable high-performance cathode materials for lithium-ion batteries. *Chem. Soc. Rev.* **49**, 4667–4680 (2020).
5. X. Zhong *et al.*, Engineering Pt and Fe dual-metal single atoms anchored on nitrogen-doped carbon with high activity and durability towards oxygen reduction reaction for zinc-air battery. *Appl. Catal. B Environ.* **286**, 119891 (2021).
6. K. Chen *et al.*, The stabilization effect of CO_2 in lithium-oxygen/CO_2 batteries. *Angew. Chem. Int. Ed. Engl.* **59**, 16661–16667 (2020).
7. B. Liu *et al.*, Recent advances in understanding Li-CO_2 electrochemistry. *Energy Environ. Sci.* **12**, 887–922 (2019).
8. A. Ahmadiparidari *et al.*, A long-cycle-life lithium-CO_2 battery with carbon neutrality. *Adv. Mater.* **31**, 1902518 (2019).
9. B. Chen *et al.*, Engineering the active sites of graphene catalyst: From CO_2 activation to activate Li-CO_2 batteries. *ACS Nano* **15**, 9841–9850 (2021).
10. Y. Jiao *et al.*, Recent progress and prospects of Li-CO_2 batteries: Mechanisms, catalysts and electrolytes. *Energy Storage Mater.* **34**, 148–170 (2021).
11. Y. Wang *et al.*, Decreasing the overpotential of aprotic li-CO2 batteries with the in-plane alloy structure in ultrathin 2D Ru-based nanosheets. *Adv. Funct. Mater.* **32**, 2202737 (2022).
12. X. Yu, A. Manthiram, Recent advances in lithium-carbon dioxide batteries. *Small Struct.* **1**, 2000027 (2020).
13. K. Zhang *et al.*, Boosting cycling stability and rate capability of Li-CO_2 batteries via synergistic photoelectric effect and plasmonic interaction. *Angew. Chem. Int. Ed. Engl.* **61**, e202201718 (2022).
14. J. Li, A. Dai, K. Amine, J. Lu, Correlating catalyst design and discharged product to reduce overpotential in Li-CO_2 batteries. *Small* **17**, 2007760 (2021).
15. X. Mu, H. Pan, P. He, H. Zhou, Li-CO_2 and Na-CO_2 batteries: Toward greener and sustainable electrical energy storage. *Adv. Mater.* **32**, 1903790 (2019).
16. B. Zhao *et al.*, 2D metallic transition-metal dichalcogenides: Structures, synthesis, properties, and applications. *Adv. Funct. Mater.* **31**, 2105132 (2021).
17. X. Tian *et al.*, Correlating the three-dimensional atomic defects and electronic properties of two-dimensional transition metal dichalcogenides. *Nat. Mater.* **19**, 867–873 (2020).
18. T. Jaramillo *et al.*, Identification of active edge sites for electrochemical H_2 evolution from MoS_2 nanocatalysts. *Science* **317**, 100–102 (2007).
19. H. Wang *et al.*, High electrochemical selectivity of edge versus terrace sites in two-dimensional layered MoS_2 materials. *Nano Lett.* **14**, 7138–7144 (2014).
20. C. J. Chen *et al.*, Catalytically active site identification of molybdenum disulfide as gas cathode in a nonaqueous Li-CO_2 battery. *ACS Appl. Mater. Interfaces* **13**, 6156–6167 (2021).
21. B. Chen *et al.*, Designing electrophilic and nucleophilic dual centers in the ReS_2 plane toward efficient bifunctional catalysts for Li-CO_2 batteries. *J. Am. Chem. Soc.* **144**, 3106–3116 (2022).
22. Y. Liu *et al.*, Toward an understanding of the reversible Li-CO_2 batteries over Metal-N4-functionalized graphene electrocatalysts. *ACS Nano* **16**, 1523–1532 (2021).
23. B.-W. Zhang *et al.*, Targeted synergy between adjacent co atoms on graphene oxide as an efficient new electrocatalyst for Li-CO_2 batteries. *Adv. Funct. Mater.* **29**, 1904206 (2019).
24. Q. Wang *et al.*, Design of active nickel single-atom decorated MoS_2 as a pH-universal catalyst for hydrogen evolution reaction. *Nano Energy* **53**, 458–467 (2018).
25. H. Lin *et al.*, Electrocatalysis of polysulfide conversion by sulfur-deficient MoS_2 nanoflakes for lithium–sulfur batteries. *Energy Environ. Sci.* **10**, 1476–1486 (2017).
26. B. Chen *et al.*, Graphene-supported atomically dispersed metals as bifunctional catalysts for next-generation batteries based on conversion reactions. *Adv. Mater.* **34**, 2105812 (2022).
27. J. Hu *et al.*, Engineering stepped edge surface structures of MoS_2 sheet stacks to accelerate the hydrogen evolution reaction. *Energy Environ. Sci.* **10**, 593–603 (2017).
28. Q. Yu *et al.*, A Ta-TaS_2 monolith catalyst with robust and metallic interface for superior hydrogen evolution. *Nat. Commun.* **12**, 6051 (2021).
29. D. Kong *et al.*, Synthesis of MoS_2 and $MoSe_2$ films with vertically aligned layers. *Nano Lett* **13**, 1341–1347 (2013).
30. H. He *et al.*, MoS_2/TiO_2edge-on heterostructure for efficient photocatalytic hydrogen evolution. *Adv. Energy Mater.* **6**, 1600464 (2016).
31. Z. Hu *et al.*, Hierarchical Ti_3C_2Tx MXene/carbon nanotubes for low overpotential and long-life Li-CO_2 batteries. *ACS Nano* **15**, 8407–8417 (2021).
32. Z. Zhang *et al.*, The first introduction of graphene to rechargeable Li–CO_2 batteries. *Angew. Chem. Int. Ed.* **54**, 6550–6553 (2015).
33. L. Diao *et al.*, An in-plane Co_9S_8@MoS_2 heterostructure for the hydrogen evolution reaction in alkaline media. *Nanoscale* **11**, 21479–21486 (2019).
34. C. Liu *et al.*, Interface engineering of MoS_2-based ternary hybrids towards reversible conversion of sodium storage. *Mater. Today Energy* **26**, 100993 (2022).
35. M. Kim *et al.*, Kirkendall effect induced bifunctional hybrid electrocatalyst (Co_9S_8@MoS_2/N-doped hollow carbon) for high performance overall water splitting. *J. Power Sources* **493**, 229688 (2021).
36. G. Y. Qiao *et al.*, Perovskite quantum dots encapsulated in a mesoporous metal-organic framework as synergistic photocathode materials. *J. Am. Chem. Soc.* **143**, 14253–14260 (2021).
37. Z. Zhang *et al.*, Verifying the rechargeability of Li-CO_2 batteries on working cathodes of ni nanoparticles highly dispersed on N-doped graphene. *Adv. Sci.* **5**, 1700567 (2018).
38. B. D. McCloskey *et al.*, Solvents' critical role in nonaqueous lithium-oxygen battery electrochemistry. *J. Phys. Chem. Lett.* **2**, 1161–1166 (2011).
39. Y. Zhang *et al.*, Single metal site and versatile transfer channel merged into covalent organic frameworks facilitate high-performance Li-CO_2 batteries. *ACS Cent. Sci.* **7**, 175–182 (2021).
40. C. Yang *et al.*, Unraveling reaction mechanisms of Mo_2C as cathode catalyst in a Li-CO_2 battery. *J. Am. Chem. Soc.* **142**, 6983–6990 (2020).
41. Z. Zhao *et al.*, Deciphering CO_2 reduction reaction mechanism in aprotic Li–CO_2 batteries using in situ vibrational spectroscopy coupled with theoretical calculations. *ACS Energy Lett.* **7**, 624–631 (2022).
42. Z. Zhao, J. Huang, Z. Peng, Achilles' heel of lithium-air batteries: Lithium carbonate. *Angew. Chem. Int. Ed.* **57**, 3874–3886 (2018).
43. L. Zhou *et al.*, Fast decomposition of Li_2CO_3/C actuated by single-atom catalysts for Li-CO_2 batteries. *Sci. China Mater.* **64**, 2139–2147 (2021).